CHAPTER VIII

FABRICATION AND CHARACTERIZATION OF NEW SEMICONDUCTING NANOMATERIALS COMPOSED OF NATURAL LAYERED SILICATES, NATURAL RUBBER, AND POLYPYRROLE

8.1 Abstract

An electrolytic admicellar polymerization was chosen for synthesizing new semiconducting nanomaterials composed of sodium montmorillonite (Na^+-MMT), polypyrrole (PPy), and natural rubber (NR). The contents of the pyrrole monomer and the Na^+-MMT were varied from 100 to 800 mM and 1 to 7 parts per hundred of rubber (phr), respectively. Fourier transform infrared spectroscopy (FTIR) and transmission electron microscopy (TEM) were used to confirm the success of the synthesis. The morphological studies carried out by X-ray diffraction (XRD) and TEM pointed out the different states of dispersion of the layered silicates, whereas the study done by scanning electron microscopy (SEM) showed a great dependence of the nanocomposite morphology on the inclusion of the layered silicates. Thermal stability studies demonstrated the thermo-protecting and thermo-oxidative behaviors imparted by the layered silicates. The mechanical and DC electrical conductivity properties were significantly improved with the inclusion of the layered silicates, especially at a 7 phr loading.

Keywords: Electrolytic admicellar polymerization; Nanocomposites; Conducting polymers

8.2 Introduction

Over the last decade, great attention has been given to electrically conducting polymers due to their excellent conductivity and potential applications in electronics, e.g. electrochemical display devices, microwave absorbing materials and electromagnetic-shields, etc. [1, 2]. Among these conducting polymers, polypyrrole (PPy) is one of the most intensively studied because of its facile synthesis, environmental stability, electrorheological (ER) property, and its superior electrical conductivity and high polarizability [3–7]. PPy can be synthesized either by chemical oxidative or the electrochemical polymerization of pyrrole in an aqueous solution, and it is the latter that provides better control of the film thickness and morphology, cleaner polymers, and better conductivity compared to the former method [3, 4]. However, the typical PPy possesses poor processability, and is insoluble, infusible, and brittle [5, 6]; such problems have limited its potential applications. The combination, therefore, of other polymers and/or inorganic materials with an organically conducting polymer, and the preparation of conducting polymer-based nanocomposites, are being extensively investigated with the expectation of overcoming these limitations.

Nanocomposites are a class of materials having a nanometer scale dispersion of reinforcing agents (at least in one dimension) [8]; and these hybrid materials often lead to superior performance in terms of mechanical strength, heat resistance, gas and solvent barrier, UV stability, etc., over individual organic polymers or conventional filled composites [5, 8]. From the development of nanoscience and nanotechnology viewpoint, the composites of PPy with nanosized inorganic materials, namely mesoporous silica [7], yttrium oxide (Y_2O_3) [9], ferric oxide (Fe_2O_3) [10], titanium dioxide (TiO_2) [11], Na^+-MMT [4–6, 12, 13], etc., have had tremendous investigation as well. Clay and clay minerals, such as sodium montmorillonite, saponite, hectorite, bentonite, etc., have been widely used in the field of nanocomposites by means of their ability to undergo cation exchange with other organic or inorganic cations to render them more organophilic and to separate them into individual layers with a very high aspect ratio. An intercalated structure is formed when the polymer chains are inserted between the clay layers; however, an

exfoliated structure is formed when the clay layers are dispersed individually within the polymer matrix. It is the latter that is often cited as the desired goal for the clay-containing composites. From the viewpoint of electrical conductivity, it has been well accepted that the electrical conductivity of PPy/MMT nanocomposites is strongly influenced by the mass loading of PPy, oxidant used for polymerization, and, more importantly, the preparation method [12]. For instance, PPy/MMT nanocomposites synthesized by electropolymerization on a gold substrate [4] showed improvement in electrical conductivity by 24 times. Whereas, PPy/MMT nanocomposites synthesized by the *in situ* polymerization of pyrrole in the presence of Na^+-MMT, dodecylbenzenesulfonic acid (DBSA) as an anionic surfactant and ferric chloride ($FeCl_3$) as an oxidant [12] and by an inverted emulsion pathway polymerization method [5, 13] using DBSA as both an emulsifier and a dopant, and ammonium persulfate (APS) as an oxidant, showed the opposite trend; i.e., the layered silicates weakened the interchain interaction of conducting PPy and impeded the delocalization of charge carriers, resulting in a decrease in electrical conductivity.

Overcoming the poor processibility of neat PPy is not easily achieved, however, although the preparation of PPy-based nanocomposites has already been studied. Thus, the utilization of moldable NR latex as a substrate for accommodating the conducting PPy film through admicellar polymerization will be an interesting task. It is suggested that the formation of an ultrathin PPy film on electrically insulating substrates like NR can overcome the poor processability of PPy and efficiently improve the electrical conductivity of NR substrates as well. Admicellar polymerization, known as a thin-film coating technique, has been applied to many polymer-substrate systems for making materials suitable for specific areas such as PPy on alumina [14, 15], nickel flake [16] and NR latex [17], and polystyrene (PS) on cotton [18], etc. This technique employs a surfactant bilayer adsorbed on a substrate surface as a soft template for the polymer film formation. Our research group has found that the admicellar polymerization of pyrrole on NR latex particles can be successfully carried out by either chemical [17] or electrochemical polymerization [19], and, very recently, the latter has been considered to be a novel approach for preparing polymer/clay nanocomposites [20]. Two important aspects, platelets exfoliation within the PPy shell and the morphological characteristics of the

synthesized nanocomposites, were verified as being influential for the improvement of their mechanical and electrical properties. It is thus anticipated that such nanocomposites will be excellent candidates for utilization as flexible smart materials for applications in static charge dissipation, biomedical and tissue engineering, etc. [21].

Despite studies focusing on the thin-film coating of PPy on a NR substrate, and the preparation of conducting PPy composites with layered silicates, no such research dealing with the admicellar polymerization of pyrrole on NR latex particles in the presence of layered silicates has been reported to date, except one from our research group [20]. Therefore, the purposes of this study are to synthesize new semiconducting nanomaterials through electrolytic admicellar polymerization and to investigate the effects of PPy and Na^+-MMT loading on the reaction progress, and the morphological and thermal properties of the nanocomposites by using various characterization techniques, e.g. FTIR, XRD, SEM, TEM, and TGA. The mechanical, dynamic thermo-mechanical and electrical properties are also examined in relation to the content of PPy and Na^+-MMT. Lastly, the formation mechanism of the electropolymerized nanocomposites is proposed.

8.3 Experimental Parts

8.3.1 Raw Materials

Natural rubber latex (60% dry rubber content) was kindly provided by Rubber Research Institute, Thailand. The pyrrole monomer ($\geq$ 97% purity) was purchased from Fluka and stored in a refrigerator at 4°C prior to use. Dodecyl sulfate sodium salt (SDS), used as an anionic surfactant, was purchased from Aldrich Co., Ltd. and was used without further purification. Pristine sodium montmorillonite (Na^+-MMT), with a cation exchange capacity (CEC) of 115 meq/100g, was kindly supplied by Kunimine Industries Co., Ltd., Tokyo, Japan, and was used as received.

8.3.2 Electrolytic Admicellar Polymerization Process

The synthesis procedure was carried out according to our previous work [19, 20]. In a typical synthesis, 25 g of centrifuged NR latex was dispersed in

an aqueous solution of SDS having an initial concentration of 16 mM with constant mechanical stirring at room temperature for at least 2 hr before adjusting the pH. As the point of zero charge (PZC) of NR is 3.9 at room temperature, the pH of the system was adjusted to 3 by using concentrated hydrochloric acid (HCl). After that, the system was equilibrated for 24 hr under stirring to ensure admicelle formation on the NR substrate. In the next step, the precooled pyrrole monomer was introduced into the equilibrated mixture to achieve the desired concentration, and the system was left again at room temperature for 1 hr to allow for the monomer adsolubilization in the admicelle. To initiate the electrochemical polymerization, a constant potential of 9 V was applied to the system using 2 cm × 10 cm copper plates as both cathode and anode electrodes. After 2 hr of polymerization, a dark admicelled rubber was synthesized and deposited at the anode electrode. It is noteworthy that, due to a corrosion effect, both electrodes were changed every 2 hr. The polymerization reaction was recorded from the start of applying a constant potential until nothing was deposited on the anode electrode. At the end of the experiment, the collected materials were twice washed with distilled water to remove the outer layer of SDS, and then dried in a vacuum oven at 70°C for 24 hr. Finally, compression molded sheets having a thickness of 3 mm were prepared for further investigation by a hydraulically operated press at 160°C for 15 min.

To synthesize the nanocomposites containing different clay loadings, 10 g of Na^+-MMT was first dispersed in 1000 ml of distilled water under vigorous stirring. Afterwards, the as-prepared suspension was added to the 16 mM SDS solution to provide the clay contents of 1, 3, 5, and 7 phr before incorporating the centrifuged NR latex and pyrrole monomer, respectively. Then, the electropolymerization was carried out using the same procedure as described above. The synthesized materials are designated as NP_x and NP_xM_y, in which N, P, and M stand for the NR, PPy, and Na^+-MMT components, respectively, and x and y represent the mass loadings of pyrrole and Na^+-MMT, respectively. The value of x varies as 100, 200, and 800 mM, and that of y varies as 1, 3, 5, and 7 phr.

8.3.3 Characterizations

8.3.3.1 Horizontal Attenuated Total Reflection-Fourier Transform Infrared Spectroscopy (HATR-FTIR)

The HATR-FTIR analysis was conducted by a Nexus 670 spectrometer in order to assess the success of the electrochemical polymerization. The spectra were recorded with 32 scans over a wave number range of 600–4000 cm^{-1} using air as a background.

8.3.3.2 X-Ray Diffraction

X-ray diffraction patterns were recorded in the range of 2θ = 1–30° (by steps of 0.02°) on an X-ray diffractometer, Bruker AXS Model D8 Discover, with Ni-filtered Cu Kα (λ = 0.154 nm) radiation operated at a tube voltage of 40 kV and a tube current of 40 mA. The basal spacing (d_{001}-spacing) was calculated using the Bragg equation:

$$\lambda = 2d\sin\theta \quad , \qquad (8.1)$$

where λ is the X-ray wavelength, d is the basal spacing, and θ is the scattering angle.

8.3.3.3 Scanning Electron Microscopy (SEM)

The morphological features of the nanocomposites were investigated using a scanning electron microscope (JEOL, Model JSM5200). The samples were fractured in a liquid nitrogen bath, placed on a sample holder using carbon adhesive tape, and then sputter-coated with gold under vacuum to prevent the electrostatic charging during observation.

8.3.3.4 Transmission Electron Microscopy (TEM)

A zero A H-7650 TEM (Hitachi High-Technologies Co., Japan), operating at an acceleration voltage of 100 kV, was used to study the dispersion of the silicate layers within the nanocomposites. Before being examined, some of the mixture collected during the electropolymerization was suspended in distilled water under sonication for 5 min to get a well-dispersed suspension. After that, a droplet was deposited on a 300 mesh copper grid and left for drying overnight. In the case of sectioning, the small specimens were cryogenically cut into ultrathin

pieces of about 75 nm thick with a diamond knife using a LEICA ULTRA CUT and were collected on the same copper grids.

8.3.3.5 Thermogravimetric Analysis (TGA) and Derivative Thermogravimetry (DTG)

TGA and DTG analyses were carried out using a Perkin-Elmer Pyris Diamond TG/DTA under nitrogen atmosphere. The weight of the samples was fixed in the range of 15–20 mg. The temperature program was set from 30°C to 600°C with a heating rate of 10°C/min. The temperature at maximum rate of weight loss taken from the DTG curve was designated as the peak decomposition temperature. The kinetics of thermal decomposition of the resulting materials was studied, and the activation energy (E_a) was calculated according to the method of Horowitz and Metzger [22, 23].

8.3.3.6 Static and Dynamic Mechanical Properties

Hardness tests were performed using a Shore A durometer according to ASTM D-2240. Tensile tests were conducted following ASTM D638M-91a with a Universal Testing Machine (LLOYD LR 100K). The conditions used for the measurements were room temperature, a crosshead speed of 50 mm/min, and a gauge length of 15 mm. Five specimens were tested and taken in an average.

Dynamic mechanical analyses were performed on a dynamic mechanical analyzer (DMA, GABO-EPLEXOR QC 25) using a constant frequency of 10 HZ and a temperature range of -80°C to +130°C. The measurements were carried out under tension mode with a static strain of 0.5% and a dynamic strain of 0.1%.

8.3.3.7 The DC Electrical Conductivity Measurement

The DC electrical conductivity (σ_{dc}) was measured at room temperature by the two-point probe technique using a Keithley 8009 Resistivity Test Fixture.

8.4 Results and Discussion

8.4.1 Morphological Characterizations

The morphology of the admicelled rubbers with different PPy loadings (NP_x) characterized by TEM is displayed in Fig. 8.1. The dark particle and pale edge represent the NR particle and the tiny PPy nodules, respectively. It can be seen from the TEM photographs that the morphology of the admicelled rubber is influenced by the mass loading of PPy. At low PPy loading (100 mM), a smooth and uniform PPy overlayer is formed on the surface of the NR core particle. This indicates that the polymerization occurs simultaneously in all initiation sites after a constant potential is applied; subsequently, the PPy layer grows gradually until it completely covers the NR core particle. Therefore, the admicelled rubber has the typical core–shell structure. At high PPy loading, especially 800 mM, one can observe that the surface of the NR particle is covered with more closely packed layers of PPy nodules, and such high PPy loading affects the growth direction of the PPy shell as well; that is, when the first layer of the PPy domains entirely covers the surface of the NR particle, or the saturation point is reached, the PPy shell tends to grow in a direction perpendicular to the surface of the NR particle and coalesces with the neighboring PPy shell of another core–shell particle to form a continuous morphology. In other words, more and more PPy nodules are presented on the surface of the NR particle as the mass loading of pyrrole increases. A similar observation has been found in the case of the preparation of core–shell particles consisting of a polystyrene–poly(ethylene glycol) monomethacrylate (PS–PEGMA) core covered with a PPy shell, as reported by Lu and coworkers [24]. As a grafted PEGMA brush-like layer was used as templates for the PPy deposition, the morphology and thickness of the PPy shell can be controlled by changing the PPy loading, by controlling the overall template surface area, and by influencing the pyrrole polymerization kinetics in the presence of different oxidants. The authors discovered that at high PPy loading, the PPy shell started to grow perpendicular to the PS-PEGMA particle surface after the saturation point had been reached, inducing an increase in the surface roughness and shell thickness of the composite particles. Compared to the present study, as the total surface area of the SDS bilayer and the

polymerization kinetics are more or less the same for all systems, changing the mass loading of PPy is considered to be the most crucial factor accounting for the difference in morphology of the admicelled rubbers. It should be noted that if the monomer concentration is not high enough and/or the polymerization occurs separately with regards to the favor of initiation sites, the resulting PPy domains will appear on the surface in the form of small islands located at a certain distance from each other [24], contributing to an inhomogeneous shell formation and an irregular conductive network. Taking the above-mentioned problem into consideration, 100 mM loading of the pyrrole monomer was chosen as the starting concentration in our study.

It is well known that the isomorphic substitutions of Al^{3+} for Si^{4+} in tetrahedral sheets and/or Mg^{2+}, Fe^{2+}, etc. for Al^{3+} in octahedral sheets within the layers are responsible for the creation of net negatively charged faces of the layered silicates which are counterbalanced by the interlayer cations, for example Na^{+}, K^{+}, etc. On the basis of the electrochemical method, both anode and cathode are marked as positive and negative electrodes, respectively, and thus the layered silicates are forced to migrate to the anode electrode along with pyrrole and NR particles during the polymerization process and are entirely encapsulated within the PPy shell. To qualitatively assess the above-mentioned scenario, TEM analyses of the corresponding nanocomposites were carried out. The TEM photographs of the NP_xM_7 nanocomposites are presented in Figs. 8.1d, 8.1e, and 8.1f. The dark lines correspond to the silicate platelets. As expected, there is an encapsulation of the layered silicates within the PPy shell for all nanocomposites in comparison with the NP_x without clay; and apparently, a smooth and uniform core–shell structure is no longer attained, i.e. there is a distortion in the uniform spherical shape of the coating layer owing to the long lateral dimension of the clay layers. This is in accordance with our previous work [20].

SEM micrographs of NP_x and the corresponding nanocomposites at 7 phr Na^{+}-MMT loading are presented in Fig. 8.2. In the absence of the clay layers, the admicelled rubbers exhibit a nice 'cauliflower-like' appearance with the uniform PPy overlayer on the surface of the NR core particle, contributing to the core–shell structure. Besides, as the PPy content increases, the surface of the NR particle is

covered with a more tightly packed layer of PPy domains, producing a more continuous morphology, which correlates well with the above TEM photographs. Since no isolated PPy particles are evidenced from the micrographs, the speculation is that the PPy domains are well attached on the surface of the NR core particle, and herein a good compatibility between NR and PPy components is achieved. Noticeably, upon the inclusion of the layered silicates, especially at 7 phr loading, the morphology of the admicelled rubber becomes more compact, rougher, and denser compared to that of the neat system. This result agrees well with the study of Liu *et al.* [4] in which the growth and assembly of PPy are evidenced not only on ordered templates provided by the clay platelets but also within the clay galleries, hence promoting the short-range ordering of the PPy chains. Taking the TEM and SEM results into consideration, the formation mechanism of the admicelled rubbers and the corresponding nanocomposites is proposed, as shown in the schematic in Fig. 8.3. As the pH was maintained at 3, pyrrole monomers are inevitably protonated, and it is suggested that the pyrrole molecules are oriented with NH^+ to the palisade region, and the hydrophobic moiety to the surfactant tail inside the bilayers through hydrophobic–hydrophobic interaction. Consequently, the highly concentrated pyrrole monomers at the solid–liquid interface will lead to the growth of the PPy layer over the NR substrate upon the introduction of a constant potential (reaction path a). Funkhouser *et al.* [14] suggested that with the formation of hydrogen bonds between pyrrole monomers and SDS head groups, the pyrrole molecules were able to insert themselves into the admicelle, and occupy space in the head group region as well. Meanwhile, an encapsulation of the clay layers inside the PPy shell can be observed via reaction path b.

8.4.2 X-Ray Diffraction Analysis

XRD patterns of the studied materials are displayed in Fig. 8.4. The basal spacing (nm) and scattering angle ($2\theta°$) are summarized in Table 8.1. Due to the well-defined layered structure, Na^+-MMT shows a diffraction peak at 2θ equal to 7.07°, which corresponds to a d_{001}-spacing of 1.25 nm (hydrated galleries). A deviation from the basal spacing of dry Na^+-MMT (0.97 nm) points to the existence of water molecules in the interlayer region [25]. For the $NP_{100}M_y$ series (not shown

here), no characteristic XRD peak is detected in the range from 2 to 10°, while, for the $NP_{200}M_y$ series (see Fig. 8.4a), a displacement of the diffraction peak towards a smaller angle is observed, and their basal spacing is larger than that of Na^+-MMT. Besides, the peak remaining at 2θ equal to 6.52° indicates that some clay tactoids coexist with the intercalated stacks, and still its height increases noticeably with the clay content, suggesting the predominance of agglomerates at higher loading [26]. Apart from the reflection at low angle, another broad peak observed in the region of 2θ = 15–25° points to the scattering of PPy chains. This can be interpreted to be that PPy is basically amorphous [5, 13]. The XRD patterns of the $NP_{800}M_y$ series are similar to that of the $NP_{200}M_y$ and so are not shown here. In fact, to attain a full understanding of the real microstructures and exfoliation levels, direct observation by TEM is required, and the results are shown in Figs. 8.1g, 8.1h, and 8.1i.

The absence of a diffraction peak from the Na^+-MMT in the $NP_{100}M_y$ series reflects a population of single platelets as well as highly disordered arrays of silicate layers, being consistent with the TEM analysis (see Fig. 8.1g). This is explained by the fact that most of the added pyrrole monomers have to diffuse into the bilayer region under the drive of favorable thermodynamics rather than being intercalated into the interlayer spacing of the silicate layers by a cation-exchange reaction with sodium cations. In this context, the synthesized PPy is expected to situate outside the silicate layers, and hence an exfoliated configuration is achieved in such system. On the other hand, in the case of the $NP_{200}M_y$ and the $NP_{800}M_y$ series, since the initial pyrrole concentration is more than sufficient to reach saturation in the bilayer [15], it would result in the intercalation of the excess protonated pyrrole between the silicate layers. In addition, on the basis of the rapid polymerization at high clay loading (see the results in section 8.4.3), those intercalated stacks, plus some tactoids, are exclusively locked up within the rigid PPy shell instead of being separated into the individual platelets by the growing PPy chains. Therefore, a mixture of intercalated stacks and small tactoids is attained at a high pyrrole mass loading, as shown in Figs. 8.1h and 8.1i.

8.4.3 Polymerization Process and Structural Characterization

Variations of the polymerization rate of the nanocomposites with the clay loading are shown in Fig. 8.5. It should be noted that the polymerization rate is calculated from the initial slope of a plot between accumulated mass at the anode electrode and polymerization time (not shown here). In the absence of the layered silicates, the reaction rate is found to increase with the mass loading of the pyrrole monomer. This is explained by the fact that the higher the pyrrole content, the greater is its concentration found at the solid–liquid interface (palisade region), giving rise to a more tightly packed PPy overlayer on the NR core particle and a high accumulated mass at the anode electrode.

When the polymerization was carried out in the presence of clay, it is obvious that the silicate layers induce two effects, i.e. catalytic and confining effects [20, 27-29], which would compete with each other during the polymerization process. As mentioned earlier, since most of the pyrrole monomers are adsolubilized into the bilayer region under the thermodynamics viewpoint, the catalytic effect constitutes the dominant role in the case of the $NP_{100}M_y$ series. Accordingly, there is a substantial increase in the reaction rate over the entire clay concentration range due to the existence of ferric ion (Fe^{3+}) in the pristine Na^+-MMT. Similar observations were found in the polymerization of an anilinium–DBSA system containing mica, talc, or Na^+-MMT [28, 29]. On the other hand, as there is a small change in the reaction rate of the $NP_{200}M_y$ and the $NP_{800}M_y$ series up to a clay loading of 3 and 5 phr, respectively, it is suggested that the confining effect becomes more pronounced within those series. This is because at higher pyrrole concentration, more protonated pyrrole is available for undergoing a cation-exchange reaction and thereafter becomes entrapped inside the clay gallery, which often results in a delay in the polymerization process [29]. But once the clay content is high enough, the catalytic effect plays the leading role again, due to an increase in the amount of ferric ion available for catalyzing the polymerization. Consequently, there is a significant increase in the reaction rate of the $NP_{200}M_y$ and the $NP_{800}M_y$ series, particularly at a 7 phr clay loading, compared to that of the neat system. However, it is suggested that such a high reaction rate, associated with the pyrrole concentration, creates a large number of intercalated PPy chains within those systems as well.

FTIR spectra were utilized for characterizing the chemical structure of the synthesized PPy, NP_x, and the corresponding nanocomposites, as shown in Fig. 8.6. The spectra of the NP_x composites (see Fig. 8.6a) display the characteristic absorption peaks of both NR and PPy components, being in good agreement with previously published values [20, 24, 30–33], and reveal that the synthesized PPy is in the doped state, as characterized by the band at 1090 cm^{-1} (δ_{N+H2}, in-plane deformation vibration of the N^+H_2). In addition, the relative intensity of the peak around 1552 cm^{-1} ($\nu_{C=C}$, pyrrole ring stretching) is consistently increased with an increasing PPy content. The spectra of the nanocomposites (see Fig. 8.6b) show a characteristic peak of Na^+-MMT at 1035 cm^{-1} corresponding to ν_{Si-O} (the Si-O stretching vibration) [34]. Besides, a remarkable shift of the band at 1090 cm^{-1} towards a lower wavenumber indicates the Coulomb interaction between the positively charged nitrogen of the protonated PPy chains and the negatively charged surfaces of the clay layers, as illustrated in Fig. 8.7.

8.4.4 DC Electrical Conductivity Measurements

The room temperature DC conductivity of the NR and HCl-doped PPy synthesized by the electrochemical method is equal to 7.18×10^{-15} and 1.69 S/cm, respectively [19], whereas, that of NP_{100}, NP_{200}, and NP_{800} is 1.73×10^{-6}, 5.4×10^{-7}, and 1.06×10^{-6} S/cm, respectively. Obviously, the electrical conductivity of NP_x composites is about eight or nine orders of magnitude higher than that of NR. This is ascribed to the continuous coating of an electrically insulating NR substrate with the conducting PPy domains as well as the formation of networks for effective charge transportation along the PPy chains [32, 35]. The plot of the DC conductivity of the nanocomposites against clay loading is given in Fig. 8.8. It was found that for the $NP_{100}M_y$ series, the electrical conductivity is increased significantly upon the introduction of the silicate layers; whereas, for the $NP_{200}M_y$ series, the electrical conductivity first decreases with increasing clay content up to a 3 phr loading and thereafter goes on increasing as the clay loading is increased up to 7 phr. However, it can be said that the conductivity of the $NP_{200}M_y$ and the $NP_{800}M_y$ series, particularly

at 5 and 7 phr clay loadings, does not change drastically when compared with that of the $NP_{100}M_y$ series.

It is clear that the physical properties, i.e. compactness and molecular orientation, and the state of dispersion of the silicate layers play a dominant role in the dependence of the electrical conductivity of the nanocomposites on the clay loading [10. 20]. For the $NP_{100}M_y$ series, as the clay platelets are dispersed in the form of a highly exfoliated structure over the entire concentration range and are mainly covered with a layer of PPy, it would create more effective networks for electron conduction [4, 6, 12, 20, 29]; for that reason, the conductivity is substantially improved. Alternatively, the confinement of the conducting PPy chains within the interlayer spaces of the Na^+-MMT reflects less electrical conductivity of the $NP_{200}M_y$ and the $NP_{800}M_y$ series, especially for the $NP_{200}M_1$ and the $NP_{200}M_3$. In this context, the clay layers weaken and disrupt the three dimensional organization of the conducting PPy chains, resulting in limited delocalization of charge carriers and in a negative influence on the electrical conductivity [5, 13, 29], even if the molecular conformation of the PPy chains in the interlayer spaces is changed from a random coil into an extended chain conformation.

8.4.5 Static and Dynamic Mechanical Properties

8.4.5.1 Mechanical Properties

Fig. 8.9a shows the tensile stress–strain curves of pure NR and NP_x composites. Note that pure NR exhibits a shore A hardness, tensile strength, and Young's modulus of 22.5, 0.5 MPa, and 0.6 MPa, respectively. Due to the rigidity of the PPy itself, the values of stress at all strain of the NP_x composites improve considerably as the mass loading of PPy increases, especially for NP_{800}, in which the stress increases initially very rapidly with strain. This indicates the ability of PPy to act as a reinforcing filler and to change the behavior of the NR from elastic to a stiff material [19, 20]. As a result, the shore A hardness, tensile strength, and Young's modulus increase in the following order $NP_{800} > NP_{200} > NP_{100}$, while their elongation at break remains less than that of pure NR. A similar trend has been observed for the polyaniline (PANI)-filled chloroprene rubber (CR) [36]. The dependence of the mechanical properties of $NP_{100}M_y$, $NP_{200}M_y$, and $NP_{800}M_y$

nanocomposites on clay loading are shown in Figs. 8.9b and 8.10. The stress–strain curves of the $NP_{100}M_y$ and $NP_{800}M_y$ series follow the same tendency as that of $NP_{200}M_y$ and so are not shown here. The results demonstrate that those mechanical properties are strongly influenced by the mass loading of Na^+-MMT. For instance, at 7 phr of the Na^+-MMT, shore A hardness, tensile strength, and Young's modulus of the $NP_{200}M_y$ nanocomposites are improved by about 40%, 160%, and 332%, respectively, compared to those of neat NP_{200}. Another important finding that is of special interest here is the positive influence of clay concentration on the elongation at break of the nanocomposites (see Fig. 8.10d). The elongation at break increases tremendously with the clay content, and the average increase is about 248%, 150%, and 86% for $NP_{100}M_7$, $NP_{200}M_7$, and $NP_{800}M_7$ nanocomposites, respectively. This illustrates the unique behavior of our synthesized materials without requiring any modification of the Na^+-MMT clay. It is well established that the pristine clay often causes a deterioration in the tensile elongation at break [37]; however, the opposite is true for a system utilizing the organoclay [38]. As the tensile strength and elongation are properties that correlate with the interfacial phase adhesion, it should be pointed out here that two crucial factors, i.e. the uniform dispersion of the clay layers and the strong interfacial adhesion between the nano-dispersed clay and the matrix, constitute the predominant mechanism for the significant improvement in those properties [36, 39-41].

8.4.5.2 Dynamic Mechanical Analysis (DMA)

DMA can be used to evaluate the reinforcing efficiency of the silicate platelets and the extent of polymer-filler interaction. Figs. 8.11a, 8.11b and 8.11c depict the variations in storage modulus (E'), loss modulus (E''), and loss tangent ($\tan\delta$), respectively, with the temperature for NP_x and the corresponding nanocomposites. Their values at different temperatures, as well as the glass transition temperature (T_g), are summarized in Table 8.2. As expected, the storage moduli of the NP_x composites increase with increasing PPy content over the whole range of temperatures. For instance, the storage moduli at T_g of NP_{200} and NP_{800} are 2.3% and 118% higher than that of NP_{100}, respectively. Such finding is in qualitative agreement with the previously discussed tensile properties in which PPy, acting as

the reinforcing filler, helps improve the stiffness of the NR. As the value of T_g is obtained from the maximum peak in the tanδ curve, it is clear that the T_g of the composites increases continuously with increasing PPy content, and their values are in an intermediate position between that of pure NR (-70°C) and PPy (97.3°C) [42, 43]. This also indicates good compatibility between the NR and PPy components. With the incorporation of the layered silicates, the E' values of the NP_xM_y systems are largely increased with the increase in clay content in the whole temperature region, especially at high Na^+-MMT loading. For instance, the E' values at T_g are improved by 770%, 1527%, and 400% for the $NP_{100}M_7$, $NP_{200}M_7$, and $NP_{800}M_7$ nanocomposites, respectively, compared to those of NP_x without clay. Again, the high stiffness of the nanocomposites is explained by the reinforcement effect of the well-dispersed layered silicates.

Normally, the interaction between the polymer matrix and the filler can be examined from the height of the tanδ peak (tanδ_{max}); that is, a reduction of the tanδ_{max} during dynamic mechanical deformation indicates the reinforcing efficiency of the corresponding filler as well as the strong interfacial adhesion between the polymer matrix and the filler, and hence the T_g is shifted towards a higher temperature because of the restricted mobility of the chain segments at the organic–inorganic interface [44, 45]. In the present study, a reduction of tanδ_{max} is clearly seen at a 7 phr loading of the layered silicates (see Fig. 8.11c), contributing to good interfacial adhesion between the polymer matrix and the clay layers. On the other hand, considering the T_g of the clay-containing composites (see Table 8.2), here the T_g values are approximately the same as those of the NP_x without clay, independently of the clay content. Such observation is similar to the studies of Das *et al.* [46] and Pradhan *et al.* [47] for MMT and its organically modified form-filled CR matrix and the layered double hydroxide (LDH)-filled carboxylated nitrile rubber (XNBR) matrix, respectively. In addition, there is a secondary peak observed at 44.6°C for the $NP_{200}M_7$ nanocomposite (see Fig. 8.11c). This is due to the relaxation of some polymer chains confined inside the silicate layers [8, 45].

8.4.6 Thermal Stability Studies

The thermal properties of the resulting materials are investigated through TGA and DTG thermograms (see Figs. 8.12 and 8.13). The corresponding values for the peak decomposition temperature ($T_{1,2}$), weight loss (%), and maximum weight loss rate (mg/min) are tabulated in Table 8.3. As can be seen, pure NR shows a sharp weight loss in the range of 300–400°C with the maximum weight loss rate at 373.6°C, while PPy shows two steps of weight loss. The initial loss below 100°C is assigned to the removal of moisture. The second loss, starting around 200°C and continuing till 550°C, is assigned to a gradual decomposition of the PPy backbone chain [4, 48]. The 66.6% residue of PPy points to the carbonization [48]. It is apparent that all NP_x composites (see Fig. 8.12a) exhibit the same decomposition patterns with two steps of weight loss. The first one around 160–300°C is due to the elimination of residual SDS [34] and the decomposition of PPy, and the second at 300–480°C results from the decomposition of the NR component [20].

For the first stage, it can be seen that the addition of the silicate layers causes a slight increase in the peak decomposition temperature (T_1) and a decrease in the weight loss of the PPy of the NP_xM_y nanocomposites in relation to the NP_x without clay. This reflects the improved thermal stability of the PPy by the well-dispersed silicate layers [40, 49]. In the second stage, which corresponds mostly to the decomposition of the NR component (designated as T_2), one can see that as the PPy content is increased, the value of the T_2 of the NP_x composites is increased accordingly, together with a decrease in the weight loss of the NR core. PPy is known for its low thermal conductivity (in the range of 0.8–1.4 $Jg^{-1}K^{-1}$) compared to other polymers, even though its electrical conductivity is very promising [50]. As a result, it is capable of being a relatively thick thermo-protective layer, providing improved thermal stability for the NR. Besides, an increase in PPy content allows more portions of the PPy molecules to be exposed to the heat, thereby resulting in an increase in the weight loss of the PPy and in the maximum weight loss rate, as well as in a decrement in the char residue (see Table 8.3).

It can be further observed that the T_2 values of the nanocomposites are slightly lower than those of the NP_x without clay. This indicates that the clay particles impart the thermo-oxidative effect to the NR matrix in which the presence

of Fe^{3+} in the octahedral sheet directly provides an oxidizing site participating in the thermal decomposition of the NR [20, 27]. On the other hand, when the maximum weight loss rate is selected as the point of comparison, one can see that the maximum weight loss rates of the nanocomposites (see Table 8.3) are less than those of the neat NP_x. This also signifies the thermo-shielding effect imparted by the well-dispersed clay platelets.

There is also a clear connection between the morphologies of the nanocomposites and their thermal properties. Since the nanocomposites from the $NP_{200}M_y$ and the $NP_{800}M_y$ series display the almost entire decomposition of PPy compared to that of the $NP_{100}M_y$ series (see Table 8.3), it is reasonable to correlate such experimental results to the difference in states of dispersion of the clay particles. That is, as the clay particles are dispersed primarily as intercalated stacks within the former systems, it makes them possess inferior thermal stability compared to that of the latter series, which contains predominantly individual platelets.

To better understand the thermal property of the studied materials, a determination of the activation energy of the decomposition process is desired with the anticipation of elucidating the role of the silicate layers on the thermal stability of the NP_xM_y nanocomposites. The decomposition activation energy (E_a) is calculated on the basis of TGA thermograms according to the Horowitz and Metzger method [22, 23]. By making the assumptions that the E_a is constant over a specific temperature range, and that the reaction follows first-order kinetics, the E_a can be calculated by the following equations:

$$\ln\{\ln[(W_0 - W_f)/(W_t - W_f)]\} = \frac{E_a \times \theta}{RT_s^2} , \qquad (8.2)$$

$$\theta = T - T_s , \qquad (8.3)$$

where W_0 is the initial weight of the sample, W_f is the final weight of the sample, W_t is the weight of the sample at the time t, R is the universal gas constant, and T_s is the reference temperature defined as the temperature where $[(W_t - W_f)/(W_0 - W_f)] = 1/e$. A plot of $\ln\{\ln[(W_0 - W_f)/(W_t - W_f)]\}$ against θ gives a straight line with the slope

equal to $\frac{E_a}{RT_x^2}$, as depicted in Fig. 8.14. By substituting our TGA data in the above equations, the E_a is calculated accordingly.

The calculated activation energy of pure NR is equal to 58.1 kJ/mol, whereas that of NP_{100}, NP_{200}, and NP_{800} is equal to 58.3, 60.0, 61.2 kJ/mol, respectively. The increment in the activation energy of the NP_x composites with increasing PPy content assures the good thermal resistance of the PPy shell, thus resulting in more energy required for the decomposition of the composites. This is in good agreement with the results described previously. The variations in the calculated activation energies of the NP_xM_y nanocomposites with clay loading are shown in Fig. 8.15. As can be seen, the activation energies of all nanocomposites decrease slightly with increasing clay content up to 3 phr, and afterwards increase with further increasing clay content, and approach the maximum value at 7 phr loading. The initial decreasing trend of E_a with clay loading points to the thermo-oxidative behavior of the clay layers, causing an acceleration in the thermal decomposition process. However, the increasing trend of E_a with further clay loading, especially at 7 phr, indicates the thermo-shielding behavior in which the well-dispersed clay layers prevents out-diffusion of the volatile decomposition products, thereby resulting in improved thermal stability of the nanocomposites. Based on the above results, it is concluded that the Na^+-MMT clay imparts both the thermo-oxidative and thermo-shielding effects to the nanocomposites at the same time. The former outweighs the latter when the clay loading is in the lower range ($\leq$ 3 phr), while an opposite trend is observed when the clay loading increases beyond 3 phr.

8.5 Conclusions

A new synthetic approach, so called 'electrolytic admicellar polymerization', was utilized for preparing new semiconducting nanocomposites based on NR, PPy, and Na^+-MMT clay using an SDS bilayer as a reaction template. The detailed formation mechanism was revealed. The influences of PPy and Na^+-MMT content on the morphology, electrical conductivity, thermal, and mechanical

properties of the synthesized nanocomposites were investigated and highlighted in detail. Based on the study of the effect of PPy content, the following conclusions can be drawn: (i) Morphology analysis revealed that a smooth and uniform PPy overlayer was attained at low loading, while the tightly packed layer was more prevalent at high loading. (ii) The reaction rate was considerably increased with mass loading of the pyrrole monomer. (iii) An increase in the electrical conductivity of the composites by eight or nine orders of magnitude compared to pure NR was directly related to the existence of continuous conductive pathways of the PPy domains. However, changes in the PPy content caused no significant difference in the electrical conductivity of the composites. (iv) The mechanical properties studies showed a reinforcing effect of PPy, as reflected by an increment in tensile strength, Young's modulus, and storage modulus of the composites with an increase in the PPy content. Also, the addition of PPy increased the T_g of the composites up to 13°C compared to the pure NR. (v) The increment in decomposition temperature (T_2) and calculated activation energy (E_a) with PPy loading pointed to the improved thermal stability of the composites.

Considering the effect of the Na^+-MMT addition, the following conclusions can be drawn: (i) XRD and TEM observations indicated the different states of dispersion of the silicate layers. The homogeneous dispersion of the clay particles as an exfoliated structure was observed in the case of the $NP_{100}M_y$ series. In contrast, for the $NP_{200}M_y$ and $NP_{800}M_y$ series, the clay particles were mainly dispersed in the forms of intercalated stacks and clay tactoids. SEM micrographs revealed a great dependence of the nanocomposite morphology on the addition of the Na^+-MMT clay; that is, the higher the amount of added Na^+-MMT, the greater the compactness of the nanocomposites. (ii) Na^+-MMT clay accelerated the polymerization reaction, particularly at a 7 phr loading. (iii) The electrical conductivity of the nanocomposites was enhanced by the addition of the Na^+-MMT clay, especially for the $NP_{100}M_y$ series. However, their value was still far below that of pure PPy under identical doping conditions. (iv) The tensile and the storage moduli of the nanocomposites were drastically increased with increasing Na^+-MMT content, which signifies the reinforcing and toughening effects of the silicate layers. However, no noticeable change in the T_g of the nanocomposites was observed. (v) The thermal

decomposition process of the nanocomposites, as evidenced by the values of calculated E_a, was accelerated when the loading of Na^+-MMT was increased up to 3 phr, while an opposite trend was found when the clay loading increased beyond 3 phr. Lastly, we anticipated that such a new synthetic approach might be extended to other conducting polymers and inorganic particles, with the expectation of attaining the synergistic effects in terms of electrical conductivity as well as thermal behavior and mechanical performance of the nanocomposites.

8.6 Acknowledgements

The authors are grateful to the Thailand Research Fund through the Royal Golden Jubilee Ph.D. Program (PHD/0088/2549), the Rachadapisek Sompoch Endowment, and Center for Petroleum, Petrochemicals, and Advanced Materials, Chulalongkorn University, for providing financial support. The authors also acknowledge Hitachi High-Technologies Corporation, Mr. Wonchalerm Rungswang, and Assoc. Prof. Suwabun Chirachanchai for performing the morphological observation via TEM zero A H-7650.

8.7 References

1. Yigit S, Hacaloglu J, Akbulut U, Toppare L. Synthetic Metals 1996;79:11-16.
2. Yigit S, Hacaloglu J, Akbulut U, Toppare L. Synthetic Metals 1997;84:205-206.
3. Sadki S, Schottland P, Brodie N, Sabouraud G. Chem. Soc. Rev. 2000;29:283-293.
4. Liu YC, Ger MD. Chemical Physics Letters 2002;362:491-496.
5. Kim JW, Liu F, Choi HJ, Hong SH, Joo J. Polymer 2003;44:289-293.
6. Boukerma K, Piquemal JY, Chehimi MM, Mravčáková M, Omastová M, Beaunier P. Polymer 2006;47:569-576.
7. Cheng Q, Pavlinek V, Li C, Lengalova A, He Y, Saha P. Materials Chemistry and Physics 2006;98:504-508.

8. Teh PL, Mohd Ishak ZA, Hashim AS, Karger-Kocsis J, Ishiaku US. European Polymer Journal 2004;40:2513-2521.

9. Cheng Q, Pavlinek V, Li C, Lengalova A, He Y, Saha P. Applied Surface Science 2006;253:1736-1740.

10. Gangopadhyay R, De A. European Polymer Journal 1999;35:1985-1992.

11. Liu YC, Huang JM, Tsai CE, Chuang TC, Wang CC. Chemical Physics Letters 2004;387:155-159.

12. Mravčáková M, Boukerma K, Omastová M, Chehimi MM. Materials Science and Engineering C 2006;26:306-313.

13. Hong SH, Kim BH, Joo J, Kim JW, Choi HJ. Current Applied Physics 2001;1:447-450.

14. Funkhouser GP, Arévalo MP, Glatzhofer DT, O'Rear EA. Langmuir 1995;11:1443-1447.

15. Yuan WL, O'Rear EA, Cho G, Funkhouser GP, Glatzhofer DT. Thin Solid Films 2001;385:96-108.

16. Genetti WB, Yuan WL, Grady BP, O'Rear EA, Lai CL. Journal of Materials Science 1998;33:3085-3093.

17. Bunsomsit K, Magaraphan R, O'Rear EA, Grady BP. Colloid Polym Sci 2002;280:509-516.

18. Pongprayoon T, Yanumet N, O'Rear EA. Journal of Colloid and Interface Science 2002;249:227-234.

19. Chirasakulkarun A. in The Petroleum and Petrochemical College; Chulalongkorn University, Bangkok: 2008.

20. Pojanavaraphan T, Chirasakulkarun A, Muksing N, Magaraphan R. Journal of Applied Polymer Science 2009;112:1552-1564.

21. Li Y, Cheng XY, Leung MY, Tsang J, Tao XM, Yuen MCW. Synthetic Metals 2005;155:89-94.

22. Horowitz HH, Metzger G. Analytical Chemistry 1963;35:1464-1468.

23. Rao PS, Subrahmanya S, Sathyanarayana DN. Synthetic Metals 2002;128:311-316.

24. Lu Y, Pich A, Adler H-J, Wang G, Rais D, Nešpůrek S. Polymer 2008;49:5002-5012.

25. Carretero-González J, Valentín JL, Arroyo M, Saalwächter K, Lopez-Manchado MA. European Polymer Journal 2008;44:3493-3500.
26. Akat H, Tasdelen MA, Prez FD, Yagci Y. European Polymer Journal 2008;44:1949-1954.
27. Pojanavaraphan T, Magaraphan R. European Polymer Journal 2008;44:1968-1977.
28. Jia W, Segal E, Narkis M, Siegmann A. Polym. Adv. Technol. 2002;13:16-24.
29. Jia W, Segal E, Kornemandel D, Lamhot Y, Narkis M, Siegmann A. Synthetic Metals 2002;128:115-120.
30. Omastová M, Trchová M, Pionteck J, Prokeš J, Stejskal J. Synthetic Metals 2004;143:153-161.
31. Blinova NV, Stejskal J, Trchová M, Prokeš J, Omastová M. European Polymer Journal 2007;43:2331-2341.
32. Cheng Q, He Y, Pavlinek V, Li C, Saha P. Synthetic Metals 2008;158:953-957.
33. Omastová M, Trchová M, Kovářová J, Stejskal J. Synthetic Metals 2003;138:447-455.
34. Yeh JM, Liou SJ, Lai CY, Wu PC. Chem. Mater. 2001;13:1131-1136.
35. Lascelles SF, Armes SP. J. Mater. Chem. 1997;7:1339-1347.
36. Saritha Chandran A, Narayanankutty SK. European Polymer Journal 2008;44:2418-2429.
37. Wang Z, Wang X, Li G, Zhang Z. Applied Clay Science 2008;42:146-150.
38. Kim JT, Oh TS, Lee DH. Polym Int 2003;52:1058-1063.
39. Liang Y, Wang Y, Wu Y, Lu Y, Zhang H, Zhang L. Polymer Testing 2005;24:12-17.
40. Hwang WG, Wei KH, Wu CM. Polymer 2004;45:5729-5734.
41. Uhl FM, Webster DC, Davuluri SP, Wong SC. European Polymer Journal 2006;42:2596-2605.
42. Chantarak S. in The Petroleum and Petrochemical College; Chulalongkorn University. Bangkok: 2007.
43. Varghese S, Karger-Kocsis J. Polymer 2003;44:4921-4927.

44. Zheng H, Zhang Y, Peng Z, Zhang Y. Polymer Testing 2004;23:217-223.

45. Teh PL, Mohd Ishak ZA, Hashim AS, Karger-Kocsis J, Ishiaku US. Journal of Applied Polymer Science 2004;94:2438-2445.

46. Das A, Costa FR, Wagenknecht U, Heinrich G. European Polymer Journal 2008;44:3456-3465.

47. Pradhan S, Costa FR, Wagenknecht U, Jehnichen D, Bhowmick AK, Heinrich G. European Polymer Journal 2008;44:3122-3132.

48. Yuvaraj H, Park EJ, Gal YS, Lim KT. Colloids and Surfaces A: Physicochem. Eng. Aspects 2008;313-314:300-303.

49. Sahoo PK, Samal R, Swain SK, Rana PK. European Polymer Journal 2008;44:3522-3528.

50. Lunn BA, Unsworth J, Booth NG, Innis PC. Journal of Materials Science 1993;28:5092-5098.

Table 8.1 X-ray scattering data of Na^+-MMT and the nanocomposites

Clay and nanocomposites	Peak position, 2θ (°)	Basal spacing, d_{001} (nm)
Na^+-MMT	7.07	1.25
$NP_{100}M_x$*	-	-
$NP_{200}M_1$	1.83	4.82
$NP_{200}M_3$	2.52, 6.71	3.50, 1.32
$NP_{200}M_5$	1.79, 6.74	4.93, 1.31
$NP_{200}M_7$	1.39, 6.52	6.33, 1.35
$NP_{800}M_1$	1.77	4.98
$NP_{800}M_3$	1.89, 6.83	4.68, 1.29
$NP_{800}M_5$	1.79, 5.53	4.93, 1.60
$NP_{800}M_7$	1.65, 5.68	5.35, 1.55

* No displacement of the diffraction peak is detected.

Table 8.2 Dynamic mechanical properties of NP_x and the corresponding nanocomposites

System	MMT content (phr)	E' [MPa] at				T_g [°C]	tan δ_{max}
		-80°C	T_g	25°C	100°C		
$NP_{100}M_y$	-	45.8	45.9	3.5	1.9	-65.9	0.63
	1	33.8	21.2	1.2	0.6	-59.8	0.61
	3	176.7	147.9	7.0	3.6	-65.8	0.62
	5	305.7	222.6	15.7	9.5	-59.6	0.47
	7	1328.5	399.3	37.5	19.9	-56.4	0.60
$NP_{200}M_y$	-	83.0	49.3	3.5	2.4	-59.4	0.69
	1	83.8	68.3	2.8	1.3	-63.2	0.77
	3	442.4	369.8	20.2	5.8	-60.1	0.49
	5	350.5	244.2	20.9	12.9	-59.8	0.56
	7	996.3	802.1	49.25	19.9	-60.0	0.33
$NP_{800}M_y$	-	151.8	100.1	9.3	6.1	-56.7	0.58
	1	887.3	105.8	3.5	2.6	-54.0	1.14
	3	3763.0	147.9	9.0	6.3	-57.8	1.04
	5	3471.0	525.9	41.2	22.5	-58.0	0.63
	7	1470.0	500.9	42.8	24.2	-56.9	0.50

Table 8.3 Summary of the thermal characteristics of the studied materials

System	Peak decomposition temperature, T_1 [a] (°C)	Weight loss [b] (%)	Peak decomposition temperature, T_2 [c] (°C)	Weight loss [d] (%)	Peak decomposition rate (mg/min)	Residue at 550°C
pure NR	-	-	373.6	93.5	2.44	1.1
PPy	260.3	22.2	-	-	0.07	68.2
NP_{100} [e]	243.2	4.7	370.2	70.3	1.63	19.6
$NP_{100}M_1$	243.7	4.6	359.0	67.1	1.45	18.7
$NP_{100}M_3$	244.6	4.5	361.9	43.4	0.77	36.5
$NP_{100}M_5$	247.1	4.4	362.0	51.9	1.47	31.1
$NP_{100}M_7$	-	13.0	380.0	71.5	1.49	8.6
NP_{200} [f]	251.7	24.6	381.1	49.8	1.84	16.1
$NP_{200}M_1$	-	24.3	378.4	60.2	1.59	5.8
$NP_{200}M_3$	-	23.9	377.0	59.9	1.34	7.8
$NP_{200}M_5$	-	23.5	374.6	62.2	1.27	8.1
$NP_{200}M_7$	-	23.1	376.1	59.8	1.31	9.1

Table 8.3 Summary of the thermal characteristics of the studied materials (continue)

System	Peak decomposition temperature, T_1 [a] (°C)	Weight loss [b] (%)	Peak decomposition temperature, T_2 [c] (°C)	Weight loss [d] (%)	Peak decomposition rate (mg/min)	Residue at 550°C
NP_{800} [g]	245.1	56.6	382.4	24.1	2.15	11.8
$NP_{800}M_1$	248.3	56.3	380.7	15.4	1.76	18.3
$NP_{800}M_3$	249.1	55.7	380.2	4.9	1.39	25.5
$NP_{800}M_5$	-	55.1	381.7	15.9	1.35	17.5
$NP_{800}M_7$	-	54.6	377.5	28.4	1.74	10.2

[a] T_1 is the decomposition temperature with regard to the PPy component.

[b] Weight loss corresponds to the PPy component.

[c] T_2 is the decomposition temperature with regard to the NR component.

[d] Weight loss corresponds to the NR component.

[e, f, g] The content of PPy used in the composites were 14, 25, and 57 wt%, respectively.

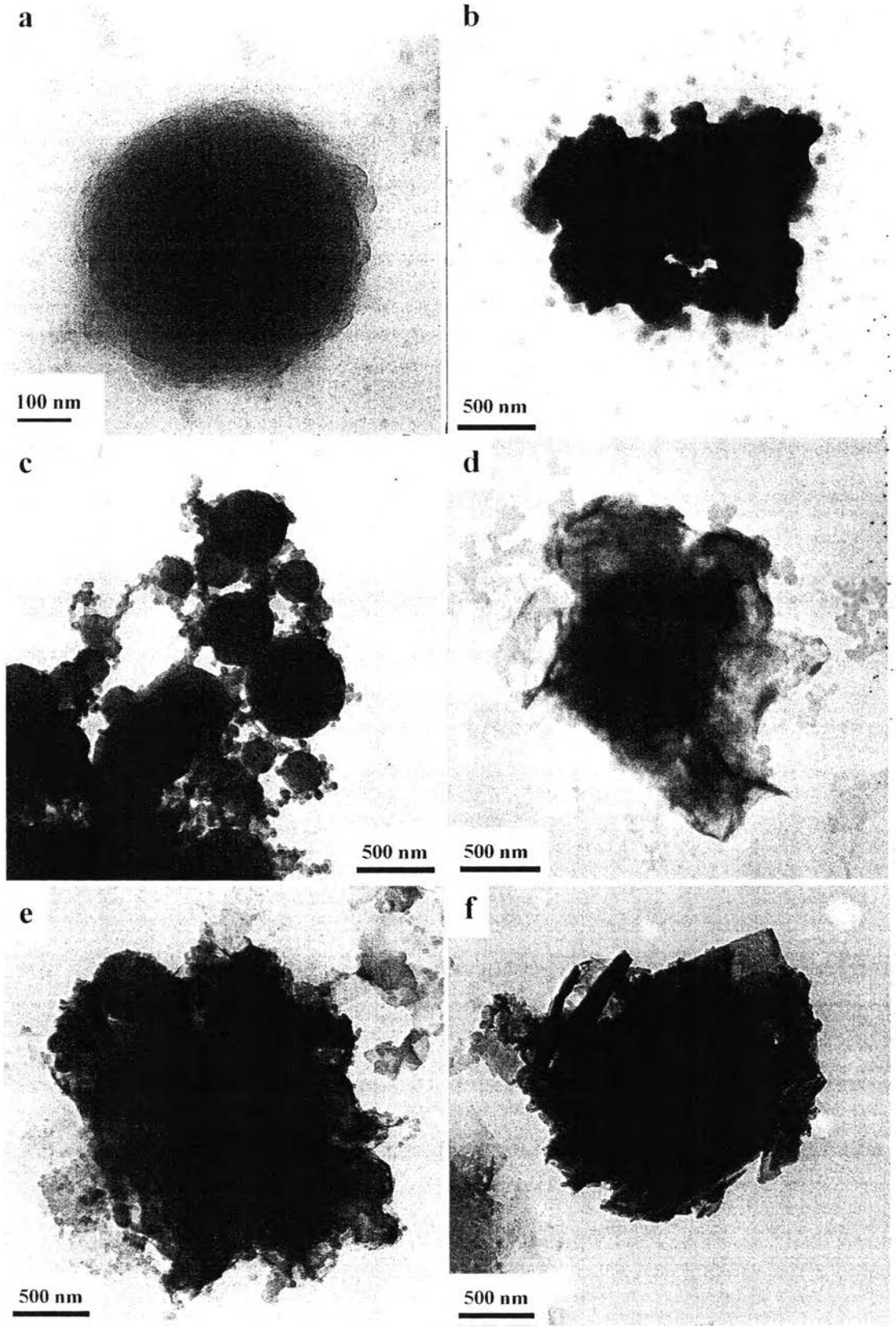
a
100 nm
b
500 nm
c
500 nm
d
500 nm
e
500 nm
f
500 nm

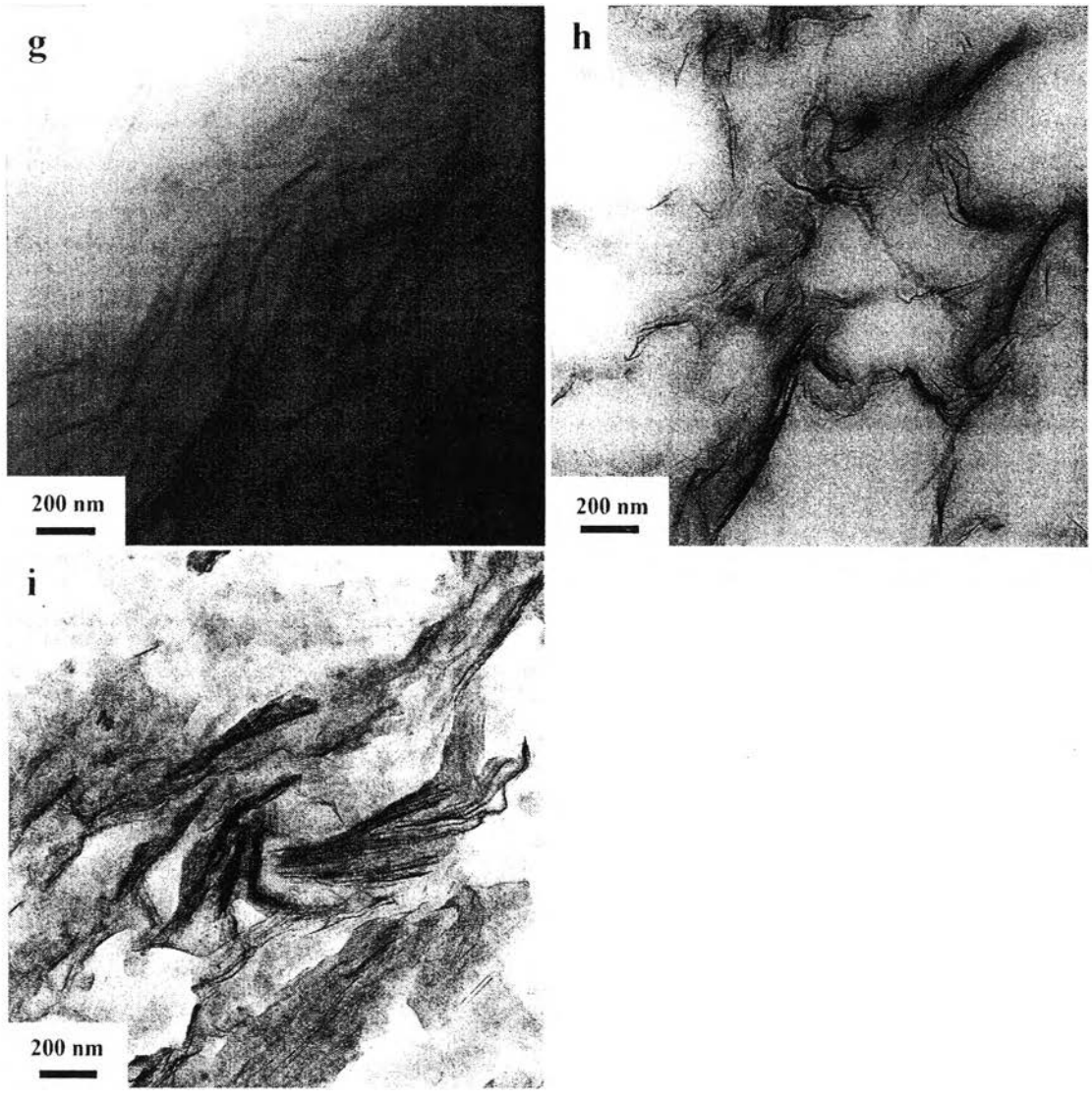

Figure 8.1 TEM images of the resulting materials: (a), (b), and (c) are micrographs of the NP_{100}, NP_{200}, and NP_{800} composites, respectively; (d), (e), and (f) are micrographs of the $NP_{100}M_7$, $NP_{200}M_7$, and $NP_{800}M_7$ samples, respectively; (g), (h), and (i) are micrographs of an ultra thin section of the $NP_{100}M_7$, $NP_{200}M_7$, and $NP_{800}M_7$ samples, respectively.

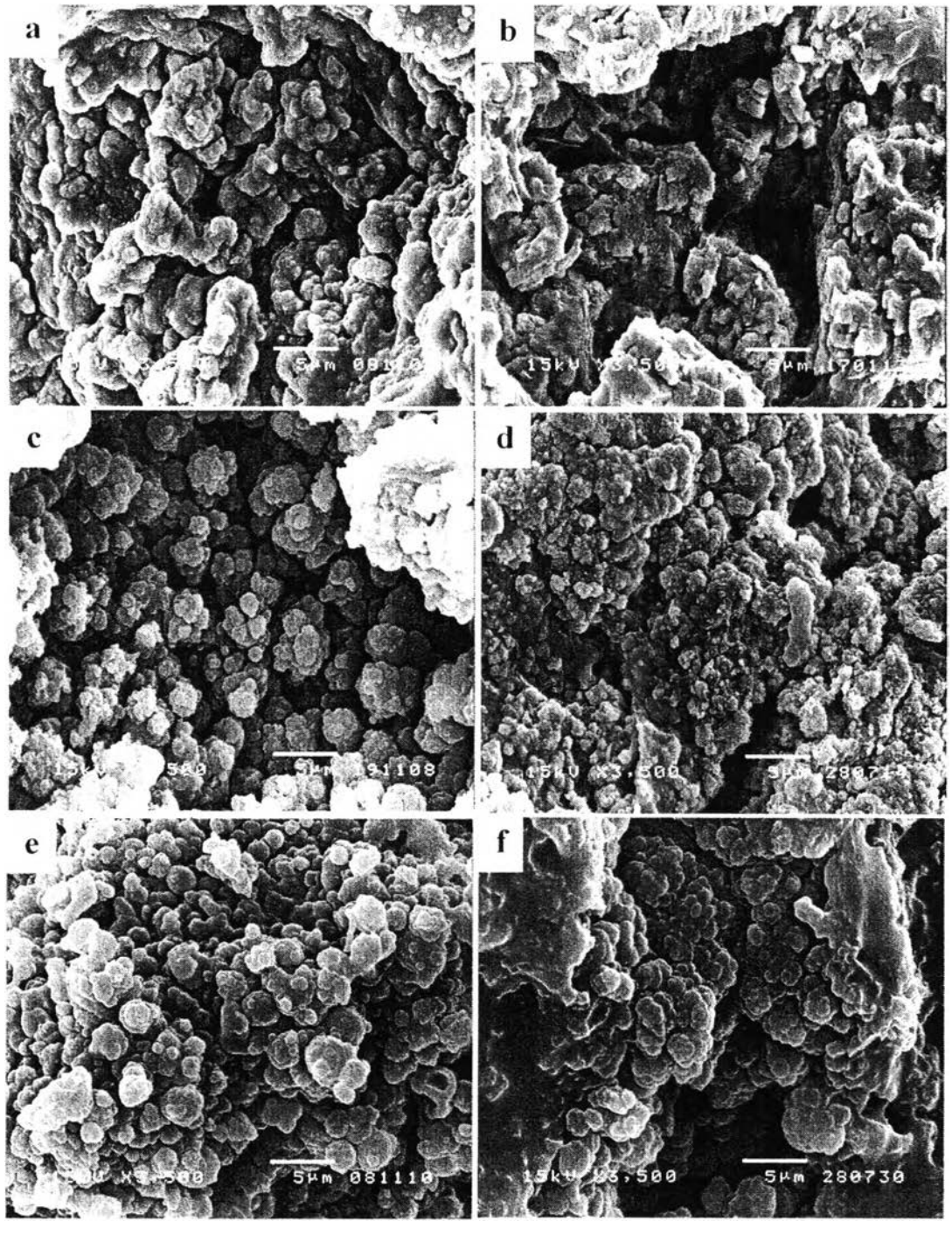

Figure 8.2 SEM micrographs of (a) NP_{100}, (c) NP_{200}, and (e) NP_{800}, with the corresponding nanocomposites (b) $NP_{100}M_7$, (d) $NP_{200}M_7$, and (f) $NP_{800}M_7$ at the same magnification (×3500).

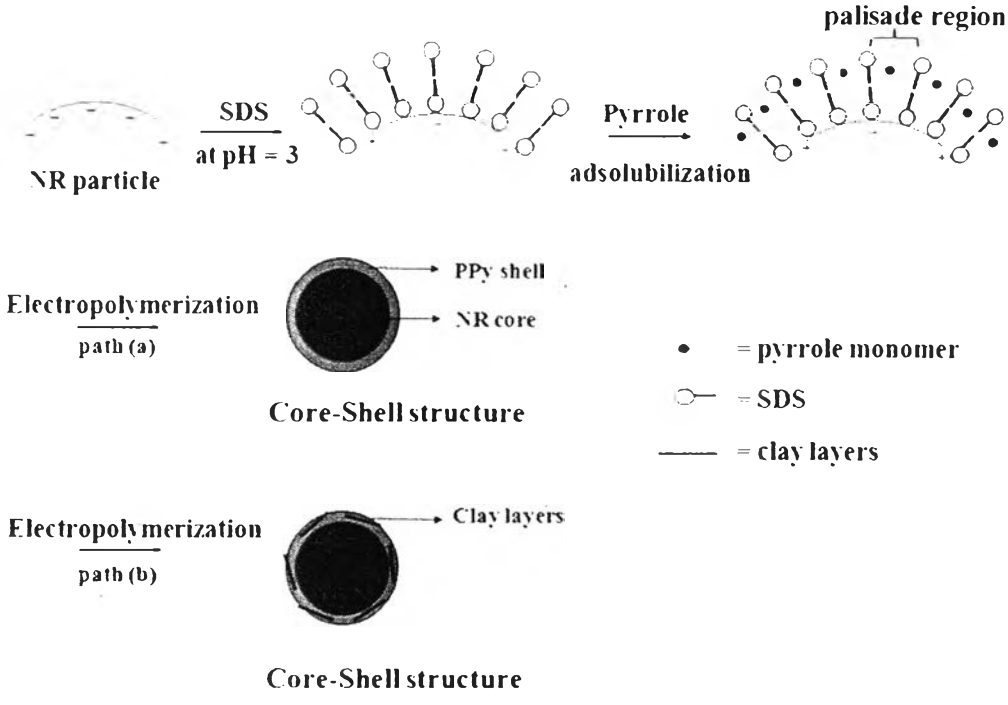

Figure 8.3 Schematic of the formation mechanism of admicelled rubbers (path a) and the nanocomposites (path b).

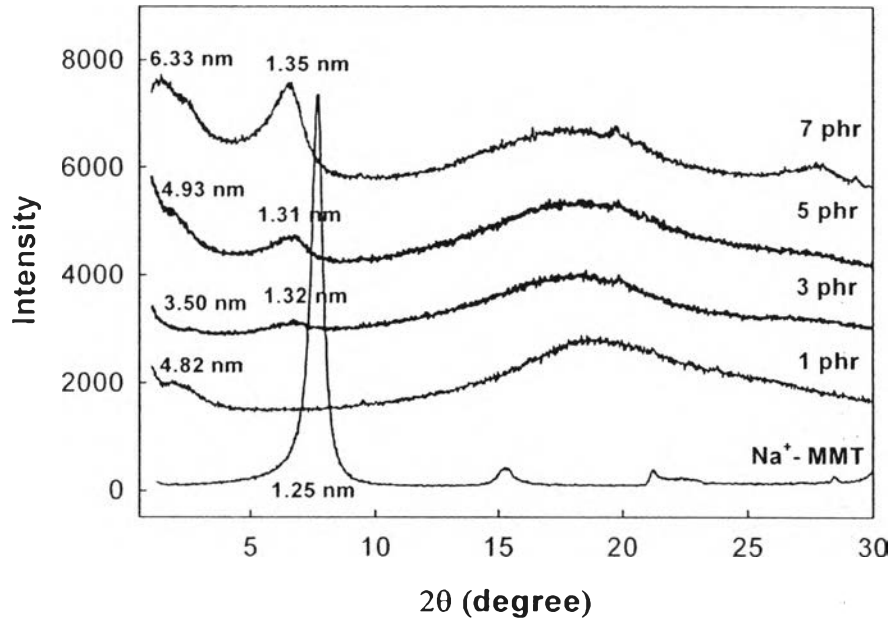

(a)

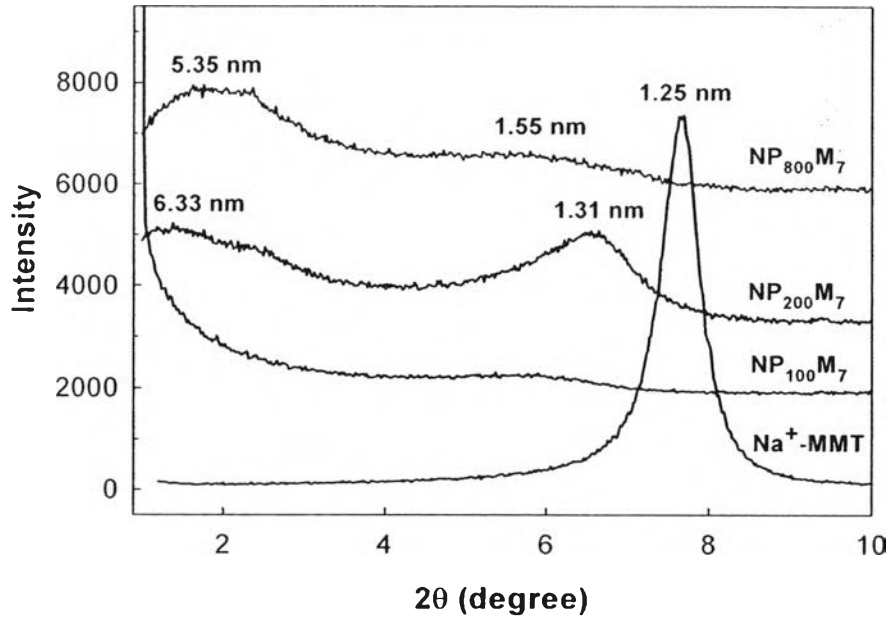

(b)

Figure 8.4 XRD patterns of (a) Na^+-MMT and $NP_{200}M_y$ series, and (b) Na^+-MMT and NP_xM_7 nanocomposites.

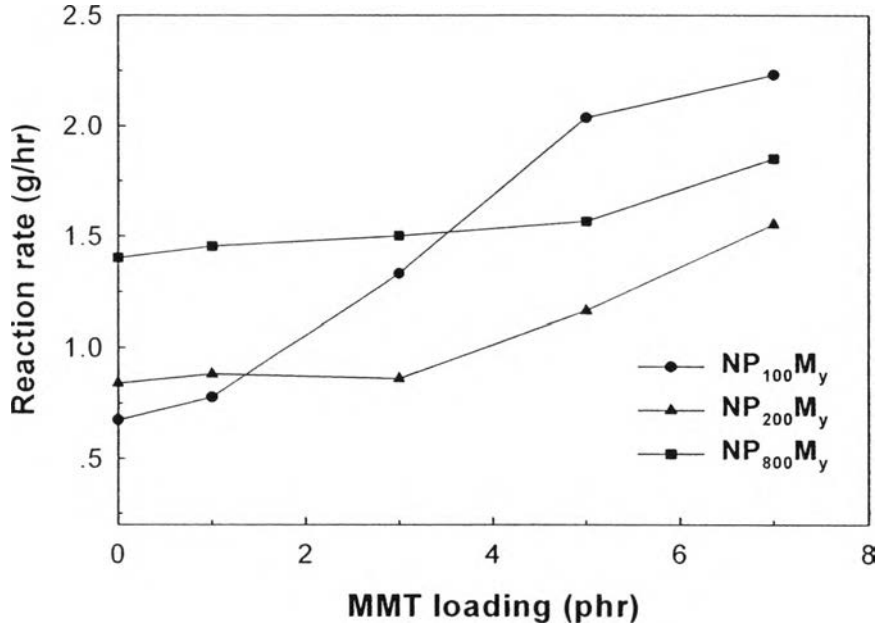

Figure 8.5 Variation of polymerization rate of the nanocomposites with the clay loading.

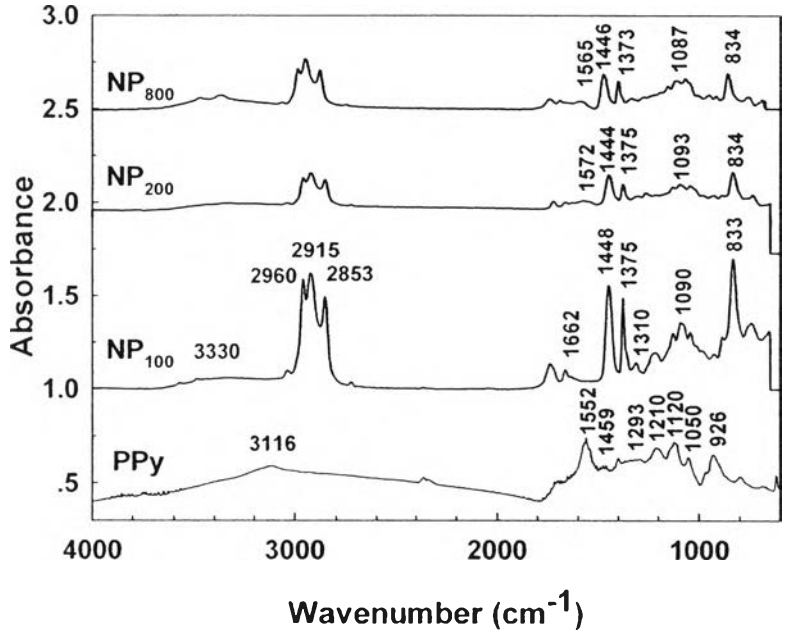

(a)

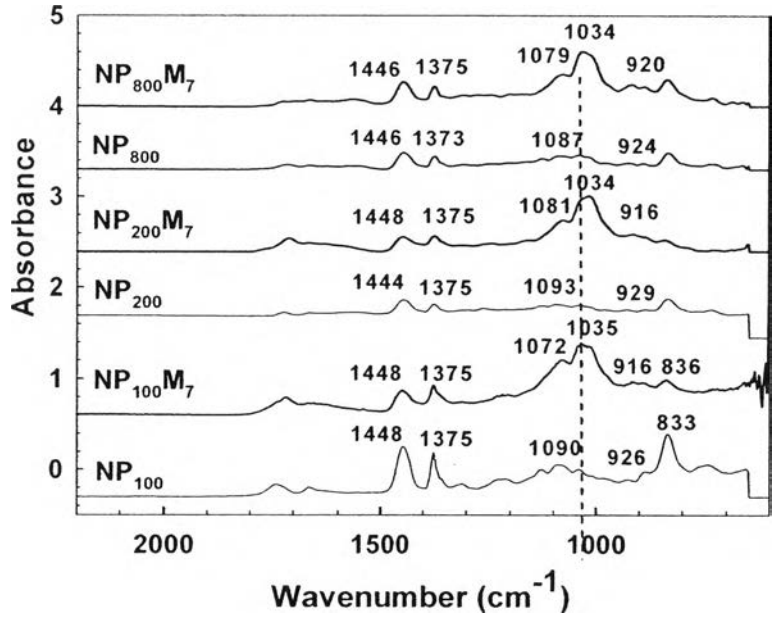

(b)

Figure 8.6 FTIR spectra of (a) PPy and NP_x composites, and (b) NP_x and NP_xM_7 nanocomposites.

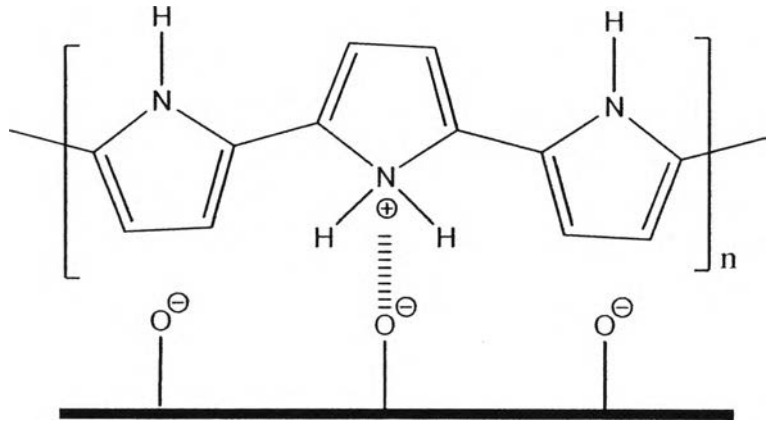

Figure 8.7 Electrostatic interaction between a protonated PPy chain and the clay layer.

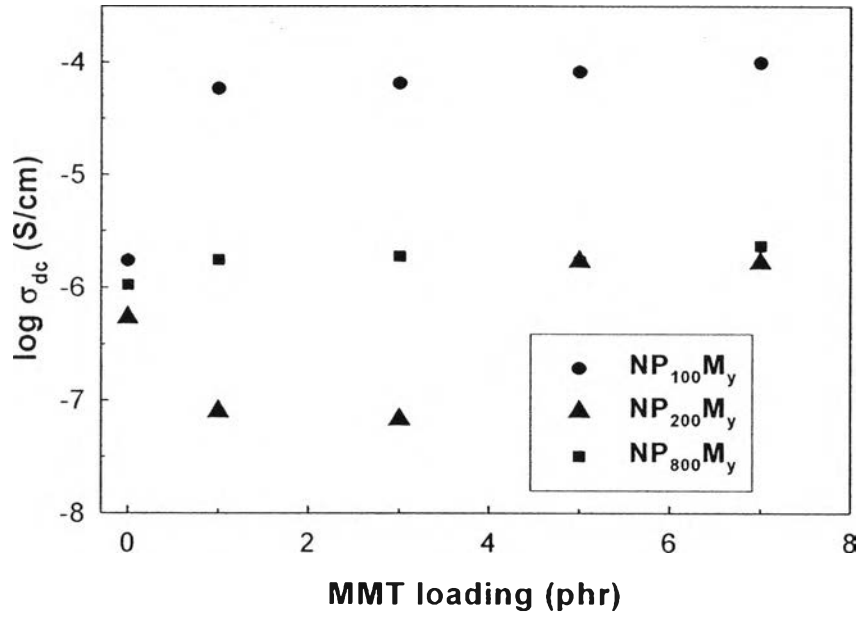

Figure 8.8 Plot of the DC conductivity against clay loading of the nanocomposites.

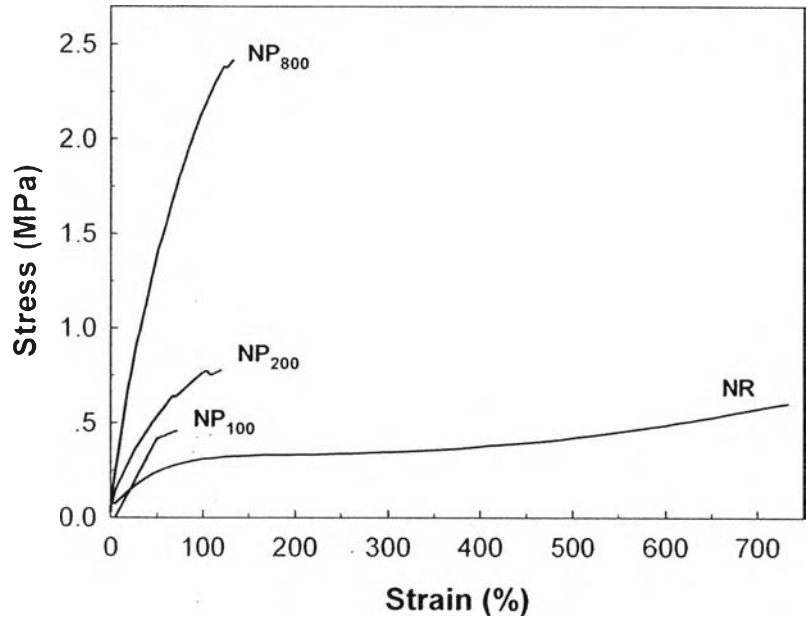

(a)

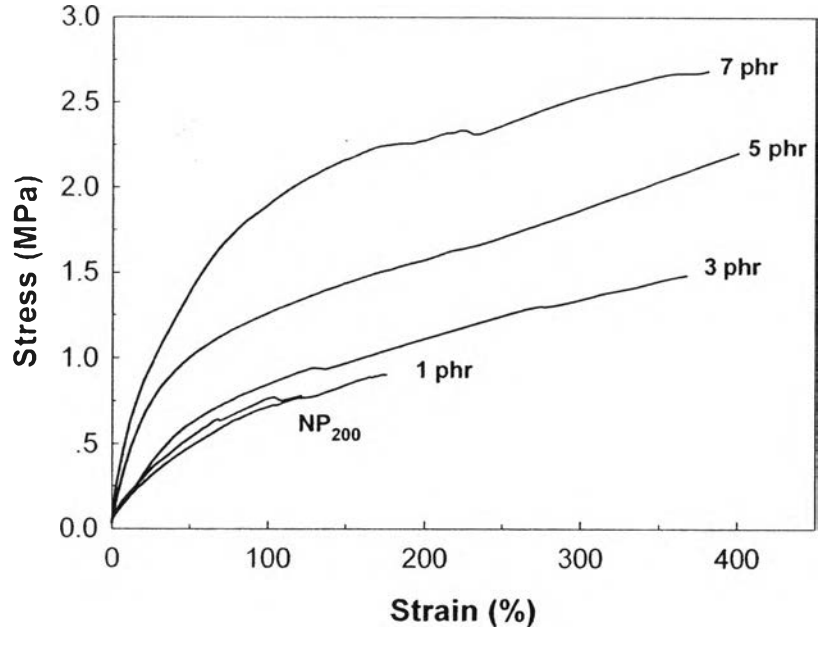

(b)

Figure 8.9 Typical stress–strain curves of (a) pure NR and NP_x composites, and (b) NP_{200} and $NP_{200}M_y$ series.

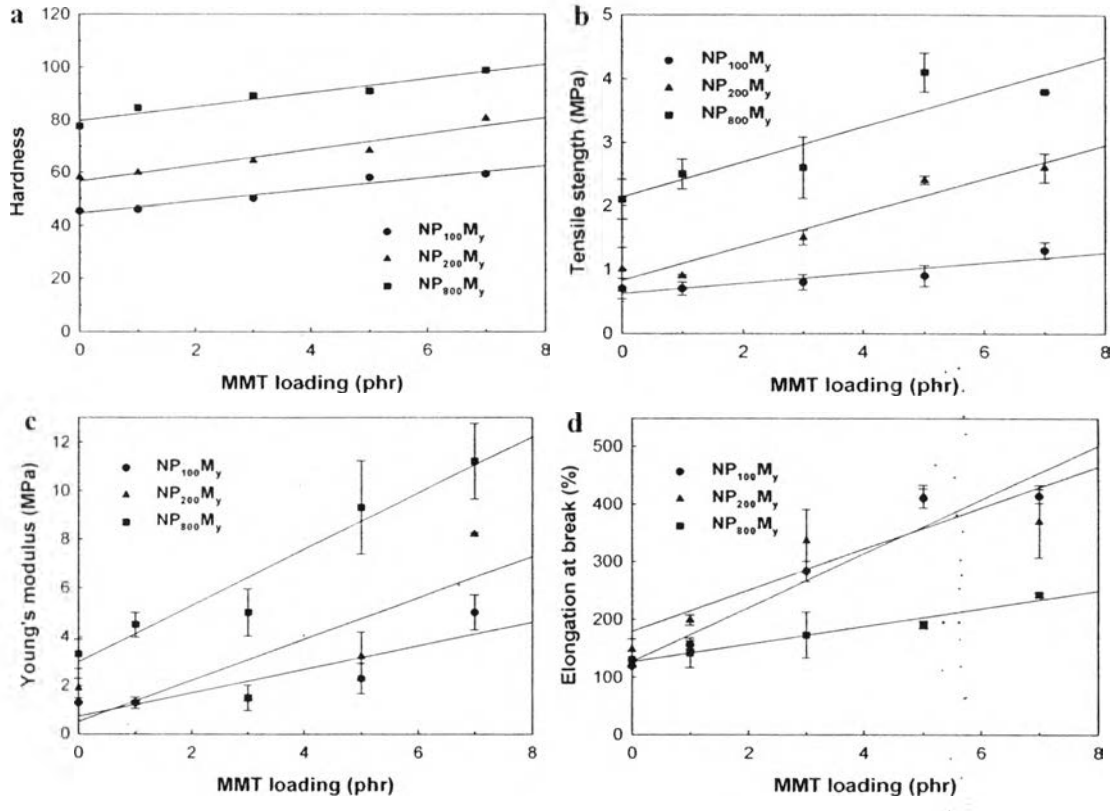

Figure 8.10 Dependence of the mechanical properties of the $NP_{100}M_y$, $NP_{200}M_y$, and $NP_{800}M_y$ series on clay loading: (a) hardness, (b) tensile strength, (c) Young's modulus, and (d) elongation at break.

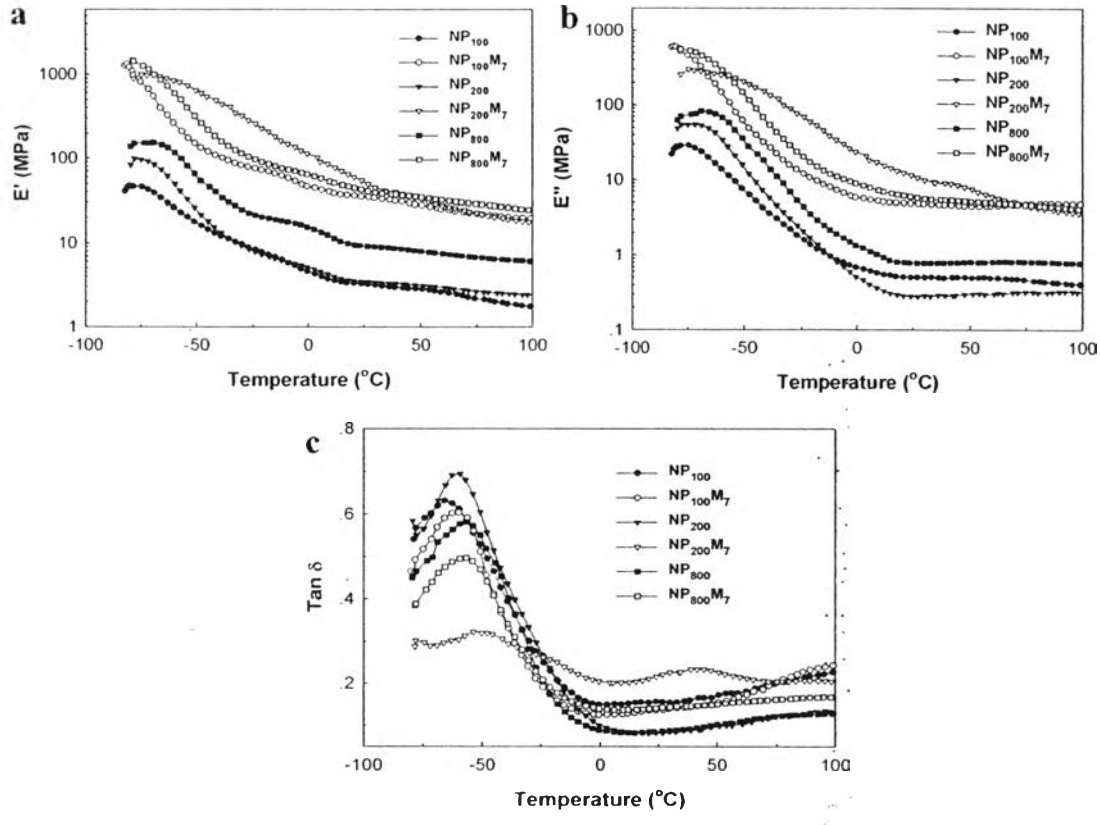

Figure 8.11 Temperature dependence of the (a) storage modulus, (b) loss modulus, and (c) loss tangent of NP_x and the corresponding nanocomposites.

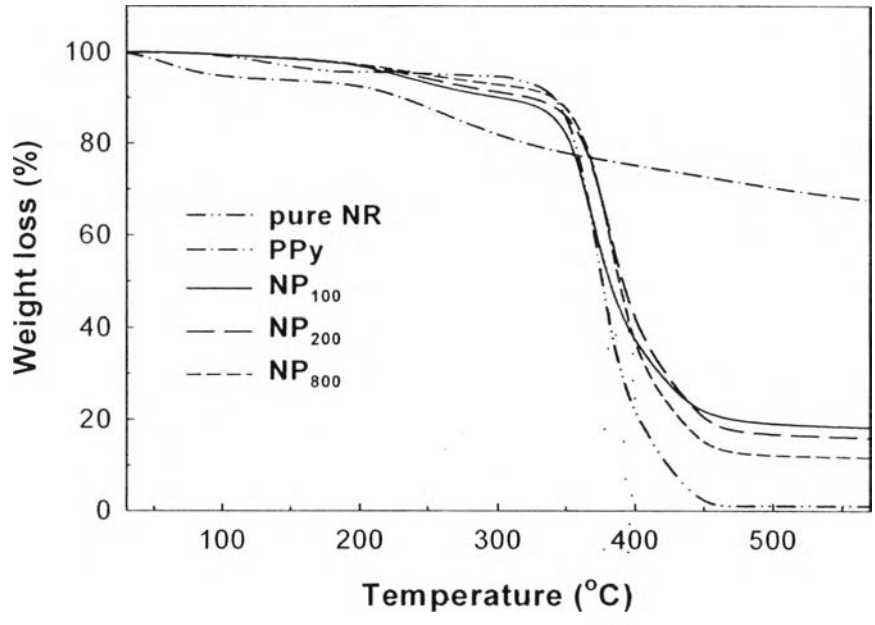

(a)

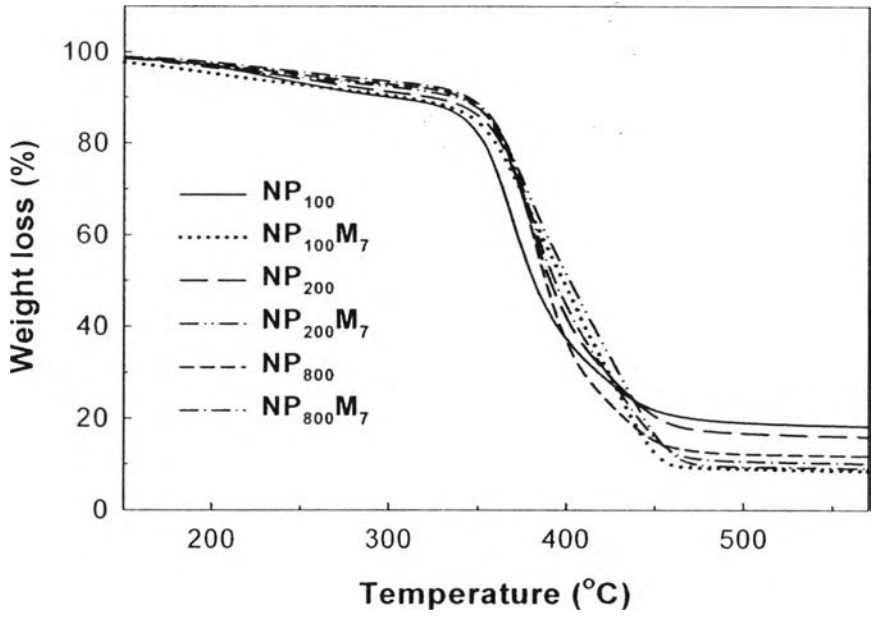

(b)

Figure 8.12 TGA curves of (a) pure NR, PPy, and NP_x composites, and (b) NP_x and NP_xM_7 nanocomposites.

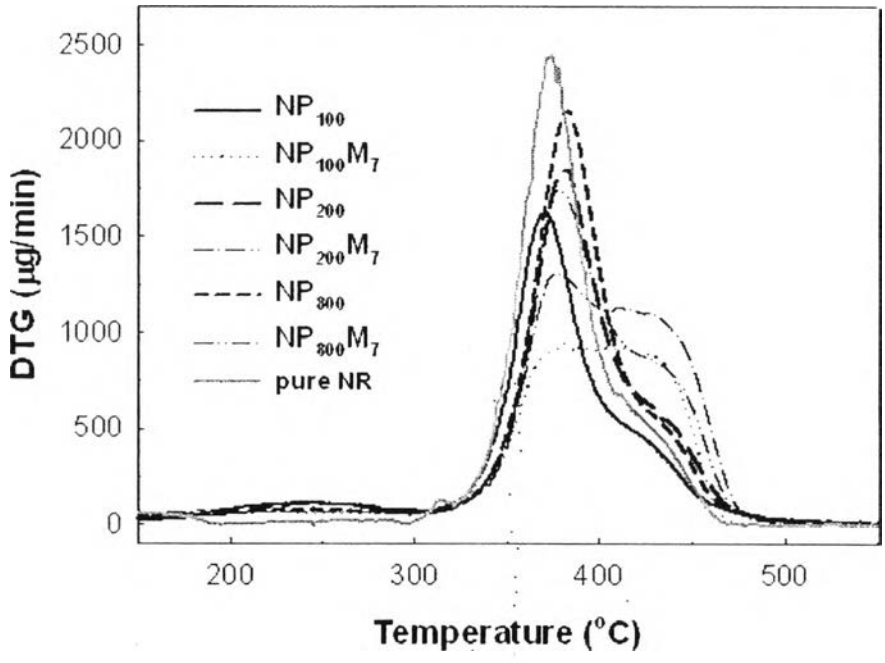

Figure 8.13 DTG curves of pure NR, NP_x, and NP_xM_7 nanocomposites.

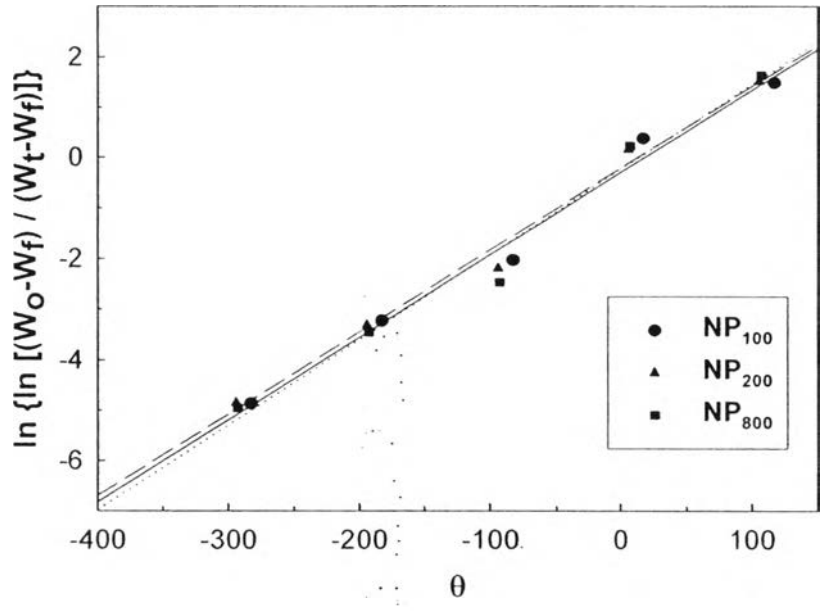

Figure 8.14 Plots of $\ln\{\ln[(W_0 - W_f)/(W_t - W_f)]\}$ against θ.

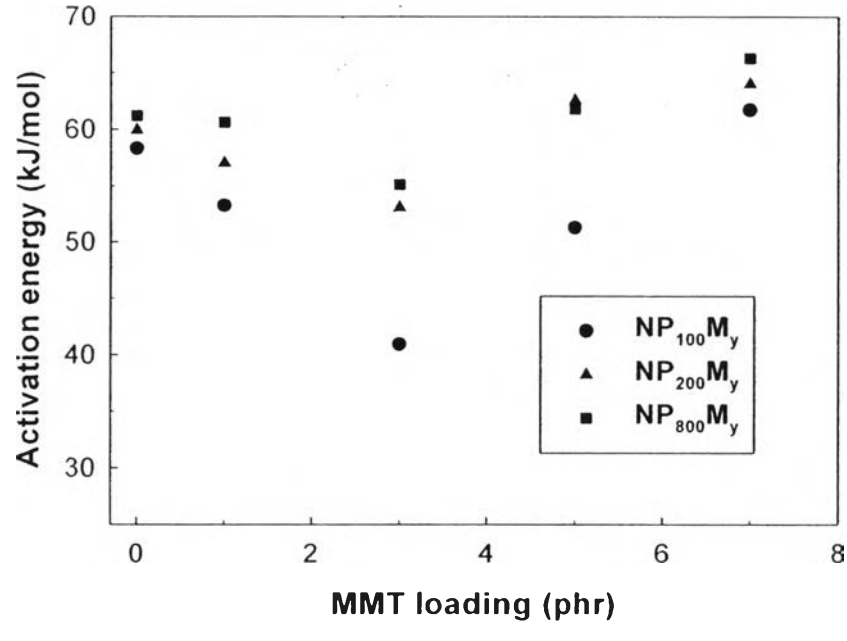

Figure 8.15 Variation of the calculated activation energy of the nanocomposites with clay loading.